AIAA Scitech 2024 Forum, 8-12 January 2024, Orlando, USA, Paper number 2024-0064
DOI: 10.2514/6.2024-0064

Implicit and Conventional Large Eddy Simulation of Flow around a Circular Cylinder at Reynolds number of 3900

Zhuoneng Li*, Andrea Da Ronch†
University of Southampton, Southampton, England SO17 1BJ, United Kingdom

Zeeshan A. Rana‡
Cranfield University, Cranfield, England, MK43 0AL, United Kingdom

The implicit Large Eddy Simulation (iLES) incorporating an unstructured 3rd-order Weighted Essential Non-Oscillatory (WENO) reconstruction method and the conventional Large Eddy Simulation with Wall Adapting Local Eddy-Viscosity (WALE) are investigated on the flow around a circular cylinder at a Reynolds number of 3900. Simulations are carried out in the framework of open-source package OpenFOAM with a 2nd-order Euler implicit time integration and Pressure-Implicit Splitting-Operator (PISO) algorithm is used for the pressure-velocity coupling. The results are compared to the high fidelity experiment and DNS data, and demonstrated a favourable performance for iLES with a 3rd-order WENO scheme on the instantaneous flow structure. The conventional LES on the prediction of mean surface pressure coefficient and velocity profiles on the wake can be beneficial by reducing the effect of Rhie-Chow interpolation. The spectral analysis reveals that the current simulations are also capturing Von Karman shedding frequencies and shear layer frequencies. Finally, distinct features of iLES and LES are discussed.

Nomenclature

ν	=	Kinematic viscosity (m^2/s)
ω	=	Weight (-)
θ	=	Circular angle (degree)
$\mathbb{A}, \mathbb{B}$	=	Scaling factor
Re	=	Reynolds number (-)
p	=	Kinematic pressure (m^2/s^2)
$\mathbf{U}$	=	Velocity vector (m/s)
t	=	Time (s)
V	=	Volume of a cell (m^3)
S	=	Area of a face (m^2)
$\mathbf{F}$	=	Surface flux (-)
$\mathbf{n}$	=	Normal unit vector of a surface
(x, y, z)	=	Cartesian coordinates
u, v, w	=	Velocity components
u', v', z'	=	Velocity fluctuations (m/s)
St	=	Strouhal number
L_r	=	Re-circulation length
f_K	=	Von Kármán frequency (-)
f_{KH}	=	Kelvin-Helmholtz frequency (-)
f_{sl}	=	Shear layer frequency (-)
f_s	=	Shedding frequency (-)
f_{sh}	=	Sub harmonic frequency (-)

*Research Fellow in Mutirotor Aerodynamics, Faculty of Engineering and Physical Sciences, zhuoneng.li@soton.ac.uk.
†Associate Professor, Faculty of Engineering and Physical Sciences, a.da-ronch@soton.ac.uk, Senior Member AIAA.
‡Senior Lecturer in Aerodynamics, Centre for Aeronautics, zeeshan.rana@cranfield.ac.uk, Member AIAA

A = Amplitude of oscillation
D = Circular cylinder diameter (m^3)
C_p = pressure coefficient
C_l = Lift coefficient (-)
C_d = Drag coefficient (-)

I. Introduction

In Computational Fluid Dynamics approaches, the Large Eddy Simulation (LES) is developed to resolve large energy-containing scales of flow while a (Sub-Grid-Scale) SGS model is employed to account for unresolved small scales. This approach captures most of the instantaneous flow features with a smaller computational cost compared to the Direct Numerical Simulation (DNS) approach [1, 2]. The main limitation for this approach is that the construction and calibration are needed for SGS models when they are applied in different flow configurations [3]. Boris [4] discovered that the leading truncation errors of the Flux-Corrected Transport (FCT) algorithm could serve as an SGS model and he recognised later [5] that several other specially designed algorithms could have the same property as well. This type of LES without an explicit SGS model is named implicit LES. The absence of explicit SGS model has advantages over conventional LES such as easier to implement and even better results can be obtained [6].

The Weighted Essentially Non Oscillatory (WENO) scheme was initially developed to capture the shock [7], its main characteristic, which achieves high order of accuracy in smooth regions while keeping the non-oscillatory property in sharp gradient regions, makes it particularly attractive in engineering applications that involve complex physics. The structured WENO scheme was employed as implcit LES to investigate the separated flow [8], where encouraging results were obtained regarding to its efficiency on capturing vortex dynamics and in the shear layer region. Following the work of Dumbser and Kaser [9] and Tsoutsanis et al.[10], the WENO scheme was extended to arbitrary mixed-element unstructured grids. Later, Tsoutsanis et al. [11] has further advanced the implicit LES application from inviscid flows [10] to viscous flows. More recently, Zeng et al [12] has demonstrated the capability of unstructured WENO scheme implemented in OpenFOAM [13] that satisfactory results can be obtained for turbulent flow with fixed separation. Following the previous work [12], the current research is motivated to carry out investigation of implicit LES on more complicated wall bounded flow.

The 2nd order Finite Volume Method (FVM) code with a collocated grid arrangement is widely used in the research, including DNS [14–16] and LES [17–19], where OpenFOAM is a representative example of such general purpose code [20]. In such code, the Rhie-Chow interpolation [21] is introduced to avoid the 'check-boarder' issue where a forth order dissipation term is added into pressure field. This process was included implicitly in OpenFOAM's implementation [22]. The drawback of it is that a significant amount of artificial dissipation is added to the numerical solution. For Reynolds Averaged Navier Stokes (RANS) simulations, this is not really a problem, however, for LES it would be relevant [23]. In addition to Rhie-Chow interpolation, Vuorinen et al [24] have identified an extra flux term in OpenFOAM implementation, which has dissipative character in absence of energy source. In fact, this 'un-documented' extra flux term is form of Choi's correction for the purpose of obtaining a converged solution that is independent of time step size [25, 26]. Here, two sources of dissipation are identified and their potential impact on the LES of wall bounded flow with separation needs to be clarified.

The flow around the circular cylinder at sub-critical Reynolds number of 3900 ($Re = UD/\nu$, where U is the free-stream flow velocity, D is the cylinder diameter and ν is the kinematic viscosity) contains co-existence of complex physics such as laminar shear layer separation, Kelvin Helmholtz instability, oscillated shedding of two shear layers and Von Karman vortex street in the wake. The interactions of three layers (two separating shear layers and wake) on the back of the cylinder make the flow highly unsteady. The first comprehensive LES study was carried out by Beaudan and Moin [27], it was found that numerical dissipation has clear impact on the small scales near wake and a non-dissipative approach is recommended for LES. Similarly, Breuer [28] pointed out a central difference scheme is more suitable for LES while upwind schemes of even higher order are not recommended because of excessive dissipation. At the very near wake, the profile of stream-wise velocity along the transverse direction, was found ressemble a U shape. This is different to experiment of Lourenco and Shih [27], where a V shape profile was obtained.

More recently, Lysenko et al [29] assessed the LES capabilities implemented in OpenFOAM, bifurcation was found as U shape velocity profile was obtained using the dynamic k-equation SGS model and the V shape profile was obtained by the Smagorinsky SGS model, the former predicted a longer recirculation length and the latter predicted a shorter length. In the study of D'Alessandro et al [30], the bifurcation seems to be SGS model dependent as the U shape velocity profile can only be predicted by the SA-IDDES model whereas SA-DES can only predict V shape profile, even

using finest grid. Chen et al [18] and Tian and Xiao [31] further investigated the influence of numerical dissipation to the shape of velocity profiles, they pointed out an over-dissipative scheme tends to turn flow into laminar and reduce re-circulation bubble and resulting a V shape profile.

Here, it can be concluded from the above literature, that the numerical dissipation and/of the type of SGS model are mainly responsible for the development of near wake region. As observed in previous studies of circular cylinder flow, the U or V shape of the near wake velocity profile can be regarded as one of indicator of numerical dissipation. Additionally, the flow past the circular cylinder is a typical model for flow of practical interest at moderate Reynolds number, well-documented studies in the literature thus provide the opportunity to assess the current implicit LES approach using OpenFOAM.

To summarise, the current research is extended from previous work [12], aims to further evaluate the performance of the implicit LES based on 3rd order WENO scheme [13], for highly unsteady wall bounded flow. The conventional LES using Wall Adapting Local Eddy Viscosity (WALE) model [32] is performed as baseline. The second aim is to investigate the potential impact of dissipation terms from the pressure-velocity coupling algorithm, since as discussed earlier, LES is sensitive to artificial numerical dissipation. The paper continues in section II with an overview of the numerical method. The section III describes the grid, boundary and initial conditions of the test case. Then the results from the time-averaged flow and instantaneous flow are analysed in section IV. Finally, the current findings are summarised with the technical contributions in the last section V.

II. Numerical Method

A. The Finite Volume Approach

Transient three dimensional incompressible flows are described by the following Navier-Stokes equations:

$$\frac{\partial \mathbf{U}}{\partial t} = -\nabla p - \nabla \cdot (\mathbf{U}\mathbf{U}) + \nu \nabla \cdot (\nabla \mathbf{U}), \tag{1}$$

where $\mathbf{U} = (u, v, w)$ is the fluid velocity vector, ν is kinematic fluid viscosity and p is kinematic pressure obtained by static pressure divided by a constant density. The incompressibility is ensured by the continuity equation:

$$\nabla \cdot \mathbf{U} = 0 \tag{2}$$

Considering a computational point C denotes the centre of a controlled volume V_i, thus the following criterion should be satisfied:

$$\int_{V_i} (x - x_C) dV_i = 0 \tag{3}$$

where x is arbitrary coordinate inside the controlled volume V_i. In the first step of finite volume discretization process, the governing equations 1 and 2 are integrated over the finite volume cell V_i with arbitrary form, such that:

$$\underbrace{\frac{\partial \mathbf{U}}{\partial t}}_{TransientTerms} = -\int_{V_i} \underbrace{(\nabla p) dV_i}_{PressureGradient} - \int_{V_i} \underbrace{\nabla \cdot (\mathbf{U}\mathbf{U}) dV_i}_{ConvectiveTerms} + \int_{V_i} \underbrace{\nu \nabla \cdot (\nabla \mathbf{U}) dV_i}_{ViscousTerms} \tag{4}$$

$$\int_{V_i} (\nabla \cdot \mathbf{U}) dV_i = 0 \tag{5}$$

It should be noted the body forces such as centrifugal force and gravity force are not counted in the general mathematical model of flow. The Gaussian theorem is then applied to transform the volume integrals of the convection, viscous and pressure gradient terms of momentum equations 4 into surface integrals such that:

$$\int_{V_i} \nabla \cdot (\mathbf{U}\mathbf{U}) dV_i = \int_S \mathbf{U}\mathbf{U} \cdot \mathbf{n} dS \tag{6}$$

$$\int_{V_i} \nu \nabla \cdot (\nabla \mathbf{U}) dV_i = \int_S \nu \nabla \mathbf{U} \cdot \mathbf{n} dS \tag{7}$$

$$\int_{V_i} (\nabla p) dV_i = \int_S p \cdot \mathbf{n} dS \tag{8}$$

The dS is a small fragment of the considered face of the controlled volume V_i and $\mathbf{n}$ denotes the surface normal unit vector. To evaluate the above surface integrals, a Gaussian quadrature is employed. The integral at a considered face of the cell is evaluated as:

$$\int_S \mathbf{F} \cdot \mathbf{n} dS = \sum_{g=1}^{N_g} (\mathbf{F} \cdot \mathbf{n})_{N_g} \omega_{N_g} S, \tag{9}$$

where g denotes an integration point and N_g is the total number of integration points along the surface and $\mathbf{F}$ denotes the surface flux. For a general purpose CFD code, such as OpenFOAM, one integration point located at the centre (a non-diagonal correction is often applied if centres of adjacent cells are not aligned) of the face is used with a weighting function $\omega_{N_g} = 1$, leading to a 2nd order overall accuracy in space, as it was found as a good balance between accuracy and computational cost[33]. The above surface integrals are treated as discrete ones and evaluated numerically through the use of Gaussian integration 9, such that:

$$\int_S \mathbf{U}\mathbf{U} \cdot \mathbf{n} dS = \sum_{j=1}^{N_{fi}} \mathbf{U}_{fi} (\mathbf{U}_{fi} \cdot \mathbf{S}_{fi}) = \sum_{j=1}^{N_{fi}} \mathbf{U}_{fi} \mathbf{F}_{fi}{}^0 \tag{10}$$

$$\int_S \nu \nabla \mathbf{U} \cdot \mathbf{n} dS = \sum_{j=1}^{N_{fi}} \nu (\nabla \mathbf{U})_{fi} \cdot \mathbf{S}_{fi} \tag{11}$$

$$\int_S p \cdot \mathbf{n} dS = \sum_{j=1}^{N_{fi}} p_{fi} \cdot \mathbf{S}_{fi} \tag{12}$$

where the subscript fi denotes the interpolated value on cell faces, $\mathbf{S}_{fi}$ denotes outward-pointing face area vector for the face fi, $\mathbf{F}^0$ represent the surface mass flux of current time step. Substituting Equations into 1 and performing a temporal discretisation lead to the general form of semi-discretized momentum equations:

$$\int_t^{t+\Delta t} \frac{\partial \overline{\mathbf{U}}_i}{\partial t} dt = \int_t^{t+\Delta t} \{\mathbf{RHS}\} \, dt \tag{13}$$

Where the **RHS** takes the following form:

$$\mathbf{RHS} = -\frac{1}{|V_i|} \sum_{j=1}^{N_{fi}} p_{fi} \cdot \mathbf{S}_{fi} - \frac{1}{|V_i|} \sum_{j=1}^{N_{fi}} \mathbf{U}_{fi} \mathbf{F}_{fi}{}^0 + \frac{1}{|V_i|} \sum_{j=1}^{N_{fi}} \nu (\nabla \mathbf{U})_{fi} \cdot \mathbf{S}_{fi} \tag{14}$$

And the $|V_i|$ is the volume of a finite volume cell, $\overline{\mathbf{U}}_i$ is cell averaged velocity which is evaluated as:

$$\overline{\mathbf{U}}_i = \frac{1}{|V_i|} \int_{V_i} \mathbf{U} dV, \tag{15}$$

Following the same procedure, a discretised continuity equations can be derived from 5:

$$\sum_{j=1}^{N_{fi}} \mathbf{U}_{fi} \cdot \mathbf{S}_{fi} = 0, \tag{16}$$

Currently, discretisation in both space and time is applied to original governing equations through finite volume method. Now, to solve the discretised system of equations on computer, a further arrangement [22] is carried out to construct a set of algebraic equations. Thus, a linear operation is required to express the surface flux of the considered cell C by its surrounding cells N, which leads to the following form:

$$a_C \mathbf{Q}_C + \sum_{j=1}^{N} a_N \mathbf{Q}_N = \mathbf{B} \tag{17}$$

where $a_C = \sum_{j=1}^{N} a_N$ contains all the time-space discretisation information of considered cell (or target cell) C while a_N contains the time-space discretisation details of all the surrounding cells of N. The rest of information is stored in **B**. The linear procedure is then applied to all the cells of the computational domain, leading to a system of algebraic equations:

$$\begin{pmatrix} a_{C1} & a_{N2} & \cdots & a_{N_n} \\ a_{N1} & a_{C2} & \cdots & a_{N_n} \\ \vdots & \vdots & \ddots & \vdots \\ a_{N_m} & a_{N2} & \cdots & a_{C_l} \end{pmatrix} \begin{pmatrix} Q_1 \\ Q_2 \\ \vdots \\ Q_n \end{pmatrix} = \begin{pmatrix} b_1 \\ b_2 \\ \vdots \\ b_n \end{pmatrix} \tag{18}$$

$$\mathbf{MQ} = \mathbf{B} \tag{19}$$

Where **M** is the coefficient matrix (which is named "lduMatrix" class in OpenFOAM), **Q** is the solution vector and **B** is the vector of boundary conditions and source terms if they are applied. Each row of the system represents the discretised equation on the considered cell C_i. Typically in OpenFOAM, the quantics of interests such as velocity are stored in the cell centre and interpolated to cell faces linearly from the adjacent cells. Any available interpolation scheme, such as linear or upwind, TVD-scheme can be applied in the specific dictionary (fvSchemes). The **M** Matrix and the **B** vector are constructed by the user-selected schemes for every control volume of the domain and is solved iteratively by user-defined method. OpenFOAM has greatly attracted the attention from engineering and academia, not only because it can provide reliable solutions but also for the wide degree of freedoms it can offer its user for customisation. Here, it is worth to be noted that in the coefficient matrix **M**, the diagonal component a_C are coefficients of the target cell or the considered cell and off-diagonal components a_N are coefficients of the surrounding cells. A split of **M** can be conducted as:

$$[\mathbf{A} + \mathbf{H}^{'}]\mathbf{Q} = \mathbf{B} \tag{20}$$

Where **A** only contains coefficients of the considered cell a_C and $\mathbf{H}^{'}$ contains only for that of the surrounding cells a_N respectively. A further arrangement leads to:

$$\mathbf{AQ} = \mathbf{B} - \mathbf{H}^{'}\mathbf{Q} \tag{21}$$

Further simplification leads to the final form of the matrix system:

$$\mathbf{AQ} = \mathbf{H} \tag{22}$$

B. Sub-Grid Scale Modelling

1. WALE SGS Model

In the context of conventional LES, an SGS model is needed to close the filtered governing equations. The explicit LES equations are obtained by applying a space filter function to Equation (13), we obtain:

$$\hat{\mathbf{U}}_t + [\hat{\mathbf{C}} - \hat{\mathbf{V}}] + \hat{\mathbf{P}} = -\nabla \cdot \tau_{sgs}, \tag{23}$$

where $\hat{\mathbf{U}}_t$ is filtered unsteady term,

$$\hat{\mathbf{U}}_t = \frac{\partial \overline{\hat{\mathbf{U}}_i}}{\partial t} dt \tag{24}$$

$\hat{\mathbf{C}}$ is filtered convective term,

$$\hat{\mathbf{C}} = \frac{1}{|V_i|} \sum_{j=1}^{N_{fi}} \hat{\mathbf{U}}_{fi} \hat{\mathbf{F}}^0_{fi} \tag{25}$$

$\hat{\mathbf{V}}$ is filtered viscous term,

$$\hat{\mathbf{V}} = \frac{1}{|V_i|}\sum_{j=1}^{N_{fi}}(\nu + \nu_{sgs})(\nabla\hat{\mathbf{U}} + \nabla\hat{\mathbf{U}}^T)_{fi} \cdot \mathbf{S}_{fi} \tag{26}$$

$\hat{\mathbf{P}}$ is filtered pressure gradient,

$$\hat{\mathbf{P}} = \frac{1}{|V_i|}\sum_{j=1}^{N_{fi}}\hat{p}_{fi} \cdot \mathbf{S}_{fi} \tag{27}$$

τ_{sgs} is the unsolved SGS stress and to be closed by a SGS model. Here, the Boussinesq assumption is adopted to model the SGS stress:

$$\tau_{sgs} - \frac{1}{3}\tau_k\delta = 2\nu_{sgs}\hat{S} \tag{28}$$

The $\hat{S}$ denotes the deformation tensor of the resolved field and ν_{sgs} is the SGS viscosity to be defined by various formulations. The Wall Adapting Local Eddy Viscosity (WALE) model of Nicoud and Ducros [32], which is well suited for LES involving wall-bounded incompressible flow and unstructured grid, is employed in the current research, such that:

$$\nu_{sgs} = C_k k_{sgs}\hat{\Delta} \tag{29}$$

The $\hat{\Delta}$ is the filter width that equals the cubic root of the cell volume, the constant C_k is set to be 0.094 and the SGS kinetic energy k_{sgs} is calculated based on the square of the velocity gradient tensor. As summarised in [32], due to the property that SGS viscosity would naturally tend to zero in the near-wall region, no damping function is needed to compute the wall-bounded flows.

2. Truncation Terms of WENO Scheme

In terms of the implicit LES approach, the unresolved turbulent eddies are represented with high-resolution convective schemes when the finite volume discretization method is applied since the original governing equations are replaced by corresponding modified equations hence truncation error terms are introduced during this process. The Modified Equation Analysis (MEA) suggests that the general form of discretized governing equations is [6]:

$$\mathbf{U}_t + [\mathbf{C} - \mathbf{V}] + \mathbf{P} = \nabla \cdot \tau(\mathbf{U}, \Delta x, \Delta t), \tag{30}$$

The leading truncation error term at the right-hand side is in the form of the divergence of a stress tensor and its similarity to Equation (23) indicates the possibility of iLES approach. For example, as demonstrated by Han [8] the leading truncation error terms for the 3rd-order WENO scheme can be expressed as:

$$\tau = -C\Delta^3 |\mathbf{F}'| \left(\frac{\partial^2\mathbf{U}}{\partial x^2}\right)^2 \left(\frac{\partial\mathbf{U}}{\partial x}\right)^{-1} \tag{31}$$

where $\mathbf{F}'$ is the flux Jacobian $\partial\mathbf{F}/\partial\mathbf{U}$ and Δ is the grid size. This way, a built-in mechanism naturally mimics the dissipative effect of an SGS model, without the need to apply additional filter nor the complicated implementation of an SGS model.

C. Time Integration

In the current research, unsteadiness is considered. To solve the time-dependent system of equations, the implicit temporal discretisation is employed. The governing equations are re-arranged that all the spatial terms are moved to the right-hand side of the equation denoted RHS:

$$\frac{\partial\overline{\mathbf{U}}_i}{\partial t} = RHS. \tag{32}$$

The system is solved by a 2nd-order time accurate backward Euler scheme:

$$\frac{\partial \overline{\mathbf{U}}_i}{\partial t} = \frac{3\overline{\mathbf{U}}_i - 4\overline{\mathbf{U}}_i^{n-1} + \overline{\mathbf{U}}_i^{n-2}}{2\Delta t}, \tag{33}$$

where n denotes the time step. Note that the order of temporal discretisation does not need to be the same as the order of spatial discretisation, the overall accuracy will be 2nd-order in this research. It should be noted, the CFL number can be larger than 1 without causing extra instability to the system, this is the primary reason that the 2nd order implicit scheme is widely used[31, 34, 35].

D. Sources of Dissipation

A closer look at the implementation in OpenFOAM source code can reveal the construction for surface flux equation:

$$phiHbyA = \underbrace{fvc :: flux(HbyA)}_{\phi_{fi}} + \underbrace{fvc :: interpolate(rAU) * fvc :: ddtCorr(U, phi)}_{\phi_c} \tag{34}$$

Where the first term ϕ_{fi} denotes the interpolated surface velocity and the second part ϕ_c is added as a flux correction term, which is not the original PISO algorithm [36], as Vuorien et al [24] first pointed out and their investigation illustrated a dissipative property of this additional flux term. Upon further dive into the detail of original implementation, the term $ddtCorr(U, phi)$ is implemented in $finiteVolume/fvc/fvcDdt.C$:

$$U.mesh().ddtScheme("ddt(" + U.name() + ')').ref().fvcDdtPhiCorr(U, phi) \tag{35}$$

In the source code of backward time scheme, $ddtSchemes/backwardDdtScheme$, the member function $fvcDdtPhiCorr(U, phi)$ is defined:

$$fvcDdtPhiCorr(U, phi) = fvcDdtPhiCoeff * \frac{1}{\Delta t} * (\phi_{old} - (\mathbf{U}_{old} \cdot S)) \tag{36}$$

And the function $fvcDdtPhiCoeff$ is defined in $ddtSchemes/ddtScheme.C$, code:

$$fvcDdtPhiCoeff = \phi - (\mathbf{U} \cdot S) \tag{37}$$

Finally the second flux correction part ϕ_c has the following form:

$$\phi_c = \frac{(\phi - (\mathbf{U} \cdot S)) * (\phi^{n-1} - (\mathbf{U}^{old} \cdot S))}{\Delta t * A_c} \tag{38}$$

In fact, this flux ϕ_c was implemented into OpenFOAM as Choi [25] and Yu et al [26] suggested additional modification to the original Rhie-Chow interpolation [21], for the purpose of removing both the time step dependency and under-relaxation factor for simulation of unsteady flows. The consequence is that the extra numerical dissipation which could deteriorate the numerical results in some contexts, as suggested by Vuorien et al [24]. Thus attention was paid to develop new numerical solver based on pressure-projection method [30, 37, 38]. On the other hand, due to the robustness of PISO algorithm and its flexibility to be coupled with various numerical schemes, it is still a widely accepted efficient method is many high fidelity numerical simulations [16, 29, 31, 39].

Following Johansson and Davidson [40], a scaling factor is introduced to limit the 4th order dissipative pressure correction terms, which are added to velocity during the Rhie-Chow interpolation procedure. Montecchia et al [41] demonstrated such reduction has a positive impact in theri wall-resolving LES conducted on channel flow. Here, a similar approach with one additional scaling factor is employed, the surface flux term ϕ_{fi} can be expressed by the following:

$$\phi_{fi} = \phi_{fi}^{HbyA} + \mathbb{A}\phi_c - \mathbb{B}\phi_{pEqn} \tag{39}$$

Where $\mathbb{A}$ and $\mathbb{B}$ are two scaling factor applied to the Choi's flux term ϕ_c and Rhie-Chow interpolation flux ϕ_{pEqn}. The following Table 1 shows the modified solvers that are employed in current investigation.

Current solver	$\mathbb{A}$	$\mathbb{B}$
piso	1	1
piso M	0	1
piso V0	0	0.5
piso V1	0	0.1

Table 1 Modified PISO solvers via two scaling factors

Case	$(\Delta\eta)_{min}/D$	$(\Delta\eta)_{avg}/D$	$\Delta\xi/D$	$\Delta z/D$
Current low resolution	1.1×10^{-3}	0.125	-	0.065
Current high resolution	1.1×10^{-3}	0.023	0.01	0.065

Table 2 Grid resolution near cylinder

III. Numerical Setup

A. Computational Domain and Grid Resolution

Various types of computational domain is used in the previous LES, O-type structured grid as Beaudan and Moin [27], Breuer [28], Kravchenko and Moin [42] and Lysenko et al [29], H-O type (H grid with an O domain around cylinder) as Franke and Frank [17], Chen et al [18] and Tian et al [31]. Cartesian grid used in Parnaudeau et al [43] and Meyer et al [19]. Hybrid unstructured grid as in Tsousantinis and Dambser [44]. The different types of domain do not seem to have a major impact to the results, as long as the flow field is well resolved. However, the span-wise resolution is subject to discussion, Breuer [28] pointed out that doubling the span-wise length to 2πD while keeping the resolution will barely impact the results.

From DNS of Wissink and Rodi [14] that very little impact on the calculation of turbulence statistics despite a span length of 8D would not completely capture the largest scale of motion in the span-wise direction. Ma et al [45] suggested a shorter re-circulation length if the spanwise length is doubled while Kravechenko and Moin [42] disagreed and claimed no significant influence is found. From the most recent LES studies, a resolution of πD/48 equivalent to a Δz $\approx$ 0.065D is adopted, see [15, 18, 29–31], their results are consistent with experiments [27, 43, 46, 47]. Besides, the computational cost needs to be taken into consideration, a doubled span-wise length increases significantly the cost while the accuracy is not comprised, therefore, it is preferred to adopt a span-wise resolution of πD/48 in current research. Note a total number of cells currently used is even smaller than Dettached Eddy Simulation (DES) [48].

An H-type grid is considered in the current work, the domain extends in the plane of 30D×20D, a schematic of the computational domain is shown in Figure 1 and two levels of grid resolution is displayed in Figure 2. As can be seen, the cells are only stretched in radial direction near the cylinder, as suggested by Wissink and Rodi [14], to avoid the numerical inaccuracies due to inadequate cell aspect ratios. Here, a lower resolution grid is used mainly to quickly assess whether the employed numerical framework is producing reliable physical results. Finite volumes cells are clustered near the cylinder in a squared O domain, with a radius of r$\approx$5D, for the purpose of capturing flow separation and getting a well-resolved flow field near the cylinder, the details are demonstrated in Table 2. The height of first cell $\Delta\eta_{min}$ on the cylinder surface is 1.1×10^{-3}D and the length $\Delta\xi = 0.01D$. According to the DNS study of Lehmkuhl et al [15], the averaged Kolmogorov length scale in the near wake is 0.02D, therefore the current high resolution grid is considered fully resolving the wall.

The space and temporal resolution is shown in Table 3, comparing with most recent LES studies of the same type of flow. A relative smaller number of total cells is used in current research, the strategy of refined grid near wall and regular grid for far-field is adopted. Most complex physics such as Kelvin Helmholtz instability, laminar separation and transition as well as the interaction of two separating shear layers (from cylinder top and bottom) take place near the cylinder, therefore most of the cells are allocated in this area with intention to accurately represent above-described physics, as its the major focus zone of current research. Besides, the flow statistics downstream largely depends on how well the flow is resolved upstream near the cylinder, as pointed out in [14, 29]. The time step for each iteration is optimised to keep a max CFL number less than 2.

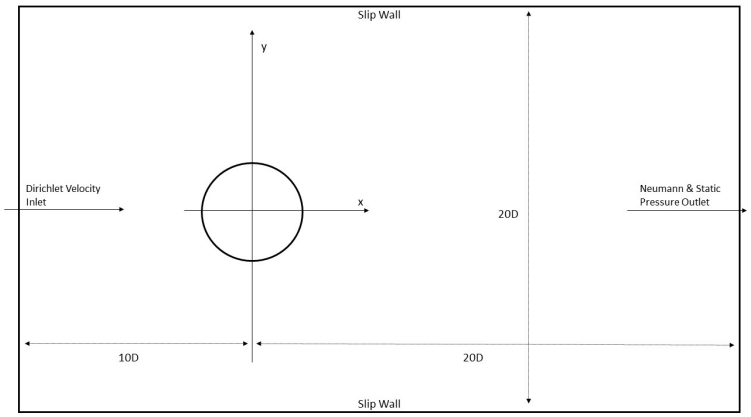

Fig. 1 Geometry of the computational domain

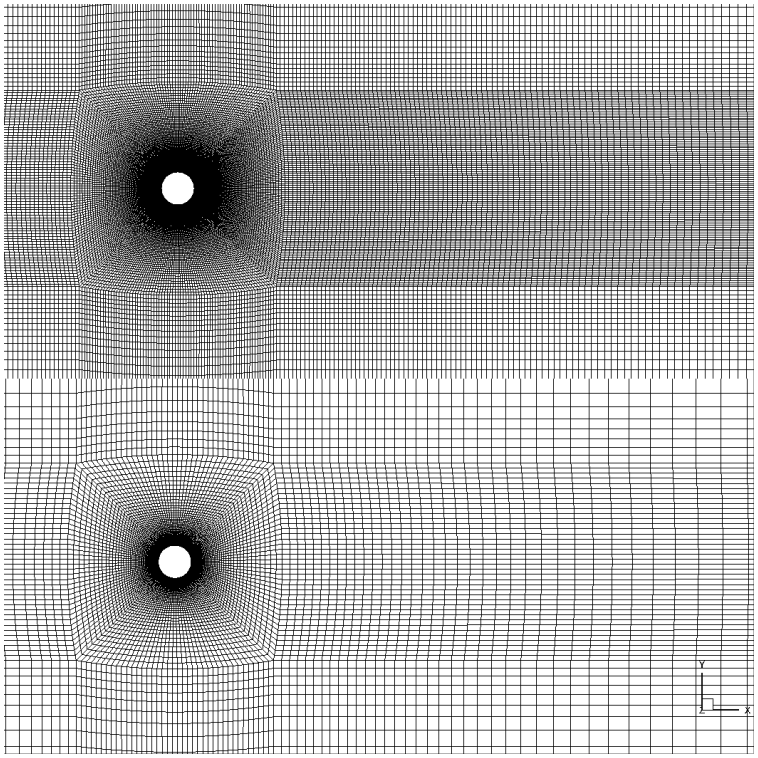

Fig. 2 High and low resolution grid

Case	Total Grid	$(\Delta\eta)_{min}/D$	Spanwise	TU/D	$\Delta t U_0/D$
Meyer et al [19]	6.5×10^6	2.5×10^{-3}	0.05D	1000	dynamic
Lysenko et al [29]	5.76×10^6	1×10^{-3}	πD/64	1400	dynamic
D'Alessando et al [30]	3.95×10^6	-	πD/48	900	0.001
Chen et al case C [18]	1.39×10^6	1.5×10^{-3}	πD/40	990	0.01
Tian et al [31]	-	1.14×10^{-3}	πD/48	300	dynamic
Current low resolution	0.9×10^6	1.1×10^{-3}	πD/48	1000	0.003
Current high resolution	3.6×10^6	1.1×10^{-3}	πD/48	1000	0.003

Table 3 General space and time resolutions and recent LES references

Case	Execution Time / Step (s)
piso WENO (iLES)	2
piso WALE (LES)	1

Table 4 Summary of computational cost for circular cylinder

B. Boundary Conditions and Flow Initialisation

A fixed velocity (Dirichlet) inlet is imposed at the inlet flow with $\mathbf{U} = (68, 0, 0)$, which corresponds a free stream Mach number of 0.2, note that no turbulence is added, as explained in [28, 29],larger grid size far upstream of the cylinder will damp the perturbations, resulting a negligible fluctuation eventually at the cylinder face. The outlet boundary is set as a hybrid condition, which switches between Neumann condition when the flow is out of the domain and a Dirichlet condition when the flow is reversing into the domain. The upper and lower surfaces in the cross-stream direction are given as slip boundary condition. To avoid any numerical uncertainties from wall function, the wall is fully resolved by the grid and no-slip wall condition is used at the cylinder surface. Periodic conditions are given at the span-wise faces.

Flow field is initiated from a steady-state RANS simulation with Spalart-Allmarass turbulence model ran for approximately 500 iterations. A conventional LES is then launched for a duration of 700 time units (TD/U_∞). Note that a duration larger than 200 time units is necessary for a statistically converged solution of the mean flow field, as pointed out by Franke and Frank [17]. From more recent LES investigations of Parnaudeau et al [43], Meyer et al[19] and Lysenko et al [29], the turbulent wake has been considered as fully established after a duration of 700 time units (equivalent to 150 shedding cycles). In this research, the flow statistics are collected about 60 shedding cycles (Note the shedding cycle is defined as $T_s = St \times TD/U_\infty$.) after quasi-steady vortex shedding is established, which corresponding approximately 300 time units. In terms of simulation time, a duration of 1000 time units corresponds 7 days simulation and there are 8 cases to run, to reduce the computational cost, the first established flow after 700 time units (5 days) obtained from conventional LES is retained as initial conditions for the rest of 7 cases, therefore, only 300 more time units (2 days) are needed each. The total computational time is reduced from 56 days to 21 days.

IV. Analysis and Discussion

A. Computational Cost

All the computations are carried out using 8 compute nodes of High-Performance Computing Service of Cranfield University, each computing node has 2 in- tel E5-2620 v4 (Broadwell) CPUs giving 16 CPU cores and 128GB of shared memory. The computational cost is concluded in the Table 4, all the simulations are conducted using 128 CPUs on the high resolution grid. A smaller variation is noticed so only standart PISO and PISO without Choi's correction are displayed. The heavy computational cost is allocated to the pre-computation for smooth indicator matrices which lasts about 1100s in average for 3rd order WENO implicit LES (denoted as iLES or piso WENO hereafter). Apart from this additional computational work, the time for each iteration for iLES is approximately twice expensive than conventional LES using WALE model (denoted as piso WALE), but the ratio is slightly reduced when more CPUs are used comparing to squared cylinder case [12], that under 64 CPUs, the iLES was almost 3 times more expensive.

B. Overall Statistics

The overall aerodynamic quantities such as cylinder back base pressure coefficient $< C_p >_b$, drag coefficients $< C_d >$, root mean square of lift coefficients $< C_l >_{rms}$, separation angle θ_{sep}, Strouhal number St and recirculation length L_r/D are summarised for all current simulations and compared with references in Table 5. All the statistics are accumulated over 60 shedding cycles after vortex shedding is stabilised.

1. Lift and Drag Coefficients

The time series of lift and drag coefficients obtained from various numerical schemes are recorded, see Figures 3 and 4. As mentioned earlier, the results from first LES with standard PISO algorithm at t*= 680TU/D (where the flow is considered established) are retained as the new initial conditions for the rest of simulations. From a closer look in the Figures 3 and 4 at t* $\approx 700TU/D$, it can be observed that changing PISO algorithm within LESs does not affect the

	Case	$< C_p >_b$	$< C_d >$	$< C_l >_{rms}$	θ_{sep}	St	L_r/D
EXP	Lourenco and Shih [27]	-	-	-	86	-	1.18
	Norberg [46]	0.89	0.99	-	-	-	-
	Parnaudeau et al [43]	-	-	-	-	-	1.51±12%
DNS	Ma et al [45]	0.765-1.04	-	-	-	0.2-0.22	1.00-1.76
	Dong et al [49]	-	-	-	-	-	1.37-1.59
	Lehmkuhl [15]	0.935	1.015	-	88	0.215	1.36
LES	Franke and Frank [17]	0.85-0.94	1.00	-	88-89	-	1.34-1.64
	Parnaudeau et al [43]	0.86	0.99	-	86	0.208	1.56
	Ouvrard et al [50]	0.78-0.94	0.90-1.02	0.051-0.219	86	0.218-0.228	1.22-1.92
	Meyer et al A [19]	1.05	1.07	-	89	0.215	1.18
	Meyer et al B [19]	0.92	1.05	-	88	0.21	1.38
	Lysenko et al A [29]	0.91	0.97	0.09	88	0.209	1.67
	Lysenko et al B [29]	0.8	1.18	0.44	89	0.19	0.9
	Tian and Xiao [31]	0.87	1.04	0.17	87	-	1.40
Current	piso WALE	1.14	1.17	0.38	86	0.213	0.91
	piso WENO	0.85	0.97	0.116	86	0.215	1.82
	piso M WALE	1.16	1.18	0.406	86	0.213	0.89
	piso M WENO	0.83	0.96	0.096	85	0.218	1.89
	piso V0 WALE	1.04	1.11	0.291	86	0.217	1.13
	piso V0 WENO	0.83	0.97	0.119	85	0.218	1.89
	piso V1 WALE	1.06	1.13	0.297	86	0.213	1.09
	piso V1 WENO	0.82	0.96	0.105	85	0.222	2.06

Table 5 Overall comparison of averaged flow quantities with some of previous experiments, DNS and LES. It is reminded that the PISO variants are introduced in the Table 1 and WENO denotes iLES, WALE denotes LES

convergence state, however, changing from LES to iLES, it took approximately a duration of 30TU/D to re-establish a quasi-converged state, as expected. This transient duration consists of 9.4% total data collection time therefore needs to be excluded during the data post-processing.

The oscillation magnitude of lift and drag coefficients of LESs are greater than those of iLES, which can be represented by the value of $< C_l >_{rms}$ displayed in the Table 5. The biggest recorded $< C_l >_{rms}$ in current research is 0.406 from LES using M PISO solver while the smallest one is 0.096 from iLES using the same solver. In LES study of Lysenko et al [29], $< C_l >_{rms}$= 0.444 is obtained for Smag SGS model and a smaller $< C_l >_{rms}$= 0.089 is reported for TKE SGS model while in Ouvrard et al [50] the $< C_l >_{rms}$ ranging from 0.051 to 0.604 depending on the SGS model and grid resolution, they they found a larger numerical viscosity from SGS model will results a higher $< C_l >_{rms}$. From experiment side, Norberg [51] has summarised previous experiments and found a large discrepancy of measured $< C_l >_{rms}$ varies from 0.03 to 0.1 at Reynolds number around 4000 - 5000, he attributes the scarceness of data to measurements of the spanwise correlation length scaled with cylinder diameter in the shedding flow, as a consequence of the complexity of two-modes turbulent shedding at this particular Reynolds number. Higher oscillation amplitude also leads to a shorter length of recirculation bubble L_r, current results are consistent previous LES simulations [29–31, 50], more details concerning the recirculation bubble L_r will be discussed in the following sections. From the results given by current simulations, it is interesting to note from PISO to M PISO algorithms, that when a large portion of the numerical dissipation of Choi's correction is completely removed, the $< C_l >_{rms}$ has becomes bigger for LES while the opposite appears for iLES. As the dissipation is further reduced from partially limiting the effect of Rhie-Chow interpolation, the LES gives a slightly smaller $< C_l >_{rms}$ and a bigger value is obtained by iLES. When the Rhie-Chow interpolation is limited to 10%, a smaller $< C_l >_{rms}$ is obtained for both LES and iLES. The oscillation amplitudes are also linked to the boundary layer transition, where the early transition produced a more chaotic separating shear layer and the wake thus higher the time variation of lift and drag. The mean drag coefficients $< C_d >$ produced by current iLESs are lower than LESs but are in good agreement with reference data, where a C_d = 0.99 with a variation of 0.05 is obtained experimentally by Norberg [46] and variation remains small between previous LES studies.

It can be observed in Figure 3 that a dominant shedding frequency f_s is located ≈ 14.7, the calculated St varies between 0.213 to 0.222 for different cases, the range is consistent with previous studies. Here, the St number is found not sensitive to numerical scheme nor grid resolution, as discussed in [28, 52], the accurate capturing of St number can not be considered as an indicator of a quality simulation. Note there is a clear sub harmonic f_{sh} peak at ≈ 43.5

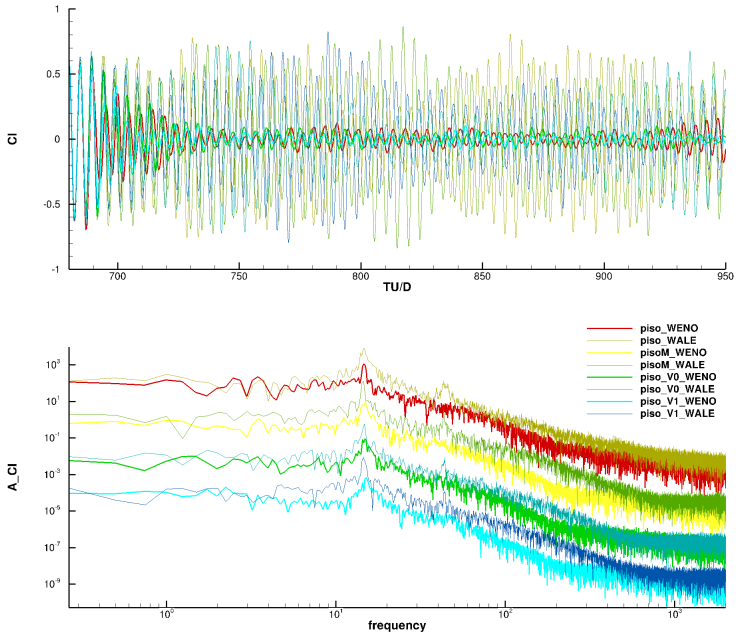

Fig. 3 Lift coefficient and its FFT

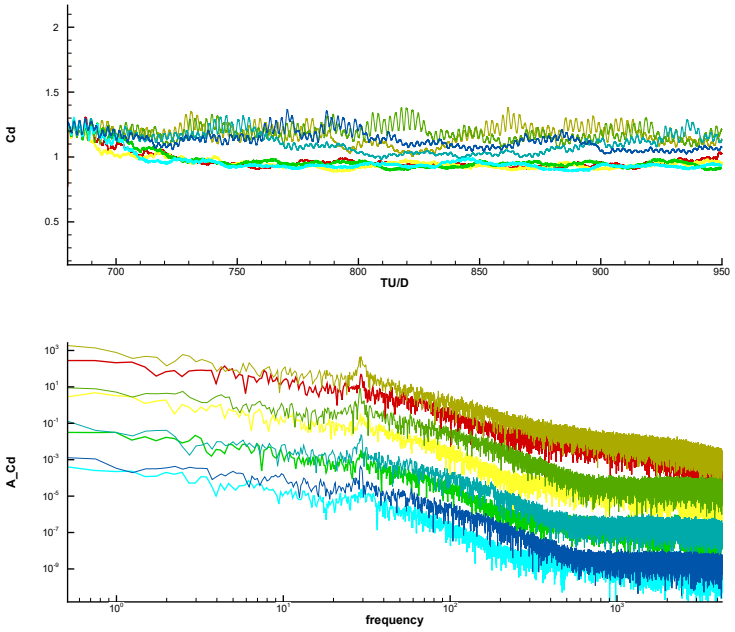

Fig. 4 Drag coefficient and its FFT

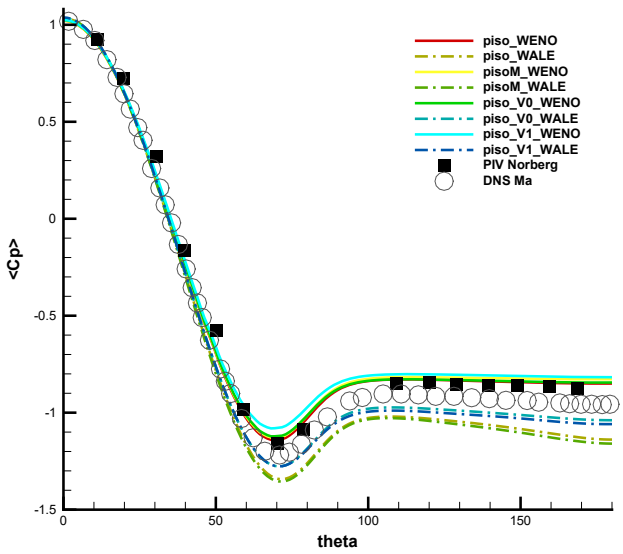

Fig. 5 Mean pressure coefficient on the cylinder surface (upper half), compared with experiment of Norberg [46] and DNS of Ma et al [45]

($f_{sh} \approx 3f_s$) for all LESs (amplified due to early transition of boundary layer, 2D to 3D, vortex breakdowns). One can see the dominant frequency for drag f_d is located at $\approx 2f_s$, it is for the same reason as for the previous squared clinder case. Less oscillated force coefficients are predicted by iLES, which means the laminar feature of the boundary layer is retained. As for the separation angle, from experiments of Lourenco and Shih [27], the separation occurs at around θ_{sep}=86, agrees well with current results and also supported by LES of Parnaudeau et al [43] and Ouvrard et al [50]. On the other hand, it is worth noting that there are simulations in the literatures [15, 17, 19, 29, 31] that give a separation angle bigger than 86. Concluding from all the experiments and simulations, the separation angle within the range of 85-90 can be considered satisfactory.

2. Pressure Distribution

Pressure coefficients C_p on the upper surface of cylinder is displayed in Figure 5. Here, the coordinates are converted to angular representation, where the $\theta = 0$ denotes the stagnation point. From the global pressure development, it can be observed that from stagnation point $\theta = 0$, the pressure continues to drop as the flow moves faster on the cylinder surface, before $\theta = 60$, there is no variation between all the current solutions and references, the min C_p is found located at $\theta = 70$ where clear derivations of simulations is seen. After the separation area, where the $\theta = 100$, the C_p converge towards a constant value, except for the LESs using full Rhie-Chow interpolation, the value to decrease $\theta = 120$, the similar trend exists in LESs of Breuer [28] (especially case C1 and D1, where no SGS is used), Lysenko et al [29] and D'alessandro et al [30]. It is found to be related to the formation of secondary vortex, which will be discussed later. Well capturing C_p min peak is an indication of well resolved boundary layer development [50]. The importance of high resolution grid near the wall is important as demonstrated in [50] that all the LESs using coarse resolution failed to capture the peak. The mean drag coefficient is highly related to pressure distribution around the cylinder, which can be seen from the Table5. The back based pressure coefficient value $< C_p >_b$ is determined as the $< C_p >$ on back side of the cylinder surface where $\theta = 180$, the calculated value from current iLES with standard PISO algorithm is $< C_p >_b$= 0.85 agrees with LES of [17, 43].

Current LES give slightly under-estimated value of $< C_p >_b$= 1.14 but tend to increase as the removal of dissipation from pressure-velocity coupling, same trend followed by iLES, particularly when the Choi's correction terms is removed and Rhie-Chow interpolation effect is reduced. As for the minimum value of C_p, the location is accurately predicted by all current simulations, however, discrepancy is observed. By modifying the standard PISO solver, the results of LES seem to be improved significantly, on the other hand, iLES predicts a better solution with the standard PISO algorithm, this could be a sign that the dissipation from pressure-velocity coupling is needed when a 3rd order WENO scheme is employed in the current test case. It is also worth noting that both LES approaches are less sensitive to Choi's correction.

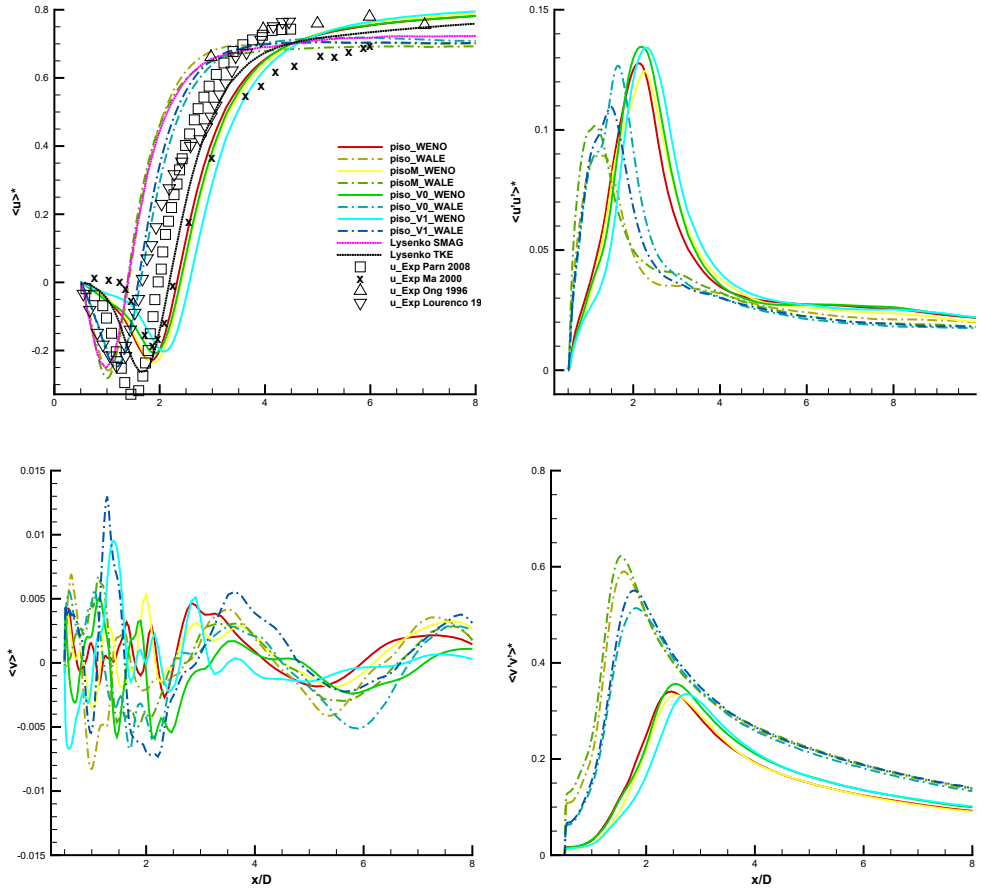

Fig. 6 Profiles of the normalized and time-averaged stream-wise velocity $\langle u \rangle$, the cross-section velocity $\langle v \rangle$ and their fluctuations $\langle u'u' \rangle$, $\langle v'v' \rangle$ on the wake centre-line. The experiment data are from Parnaudeau et al [43], Ma et al [45], Ong [47] and Lourenco [27].

C. Velocity Profiles in the Wake

In this section, the focus is on the statistics on the near wake, where most of the data scarceness of the previous studies is found in this zone. The velocity profiles and their fluctuation components are extracted at various locations. Here, only at x=1.06D is showed as discussed.

The top left in Figure 6 shows the stream-wise velocities $< u >^*$ on the wake centre-line, the value starts at 0 due to a no-slip boundary condition on the cylinder surface and tends to increase towards negative until a maximum is reached, then increase towards a positive direction, here the distance from cylinder base and the location where the velocity changing to positive, defined as re-circulation length L_r. It can be observed that the clear variance of different method mainly lies on two points: the minimum value of the stream-wise velocity u_{min} and the location of this minimum value.

The u_{min} given by LES of Lysenko et al [29] is -0.27, consistent with experiments of Lourenco and Shih [27], in the range of (-0.23,-0.26), similarly in the LES study of Parnaudeau et al [43] and iLES of Meyer et al [19], the values are falling in this range. Current results are also in agreement, apart from iLES with reduced Rhie-Chow interpolation where the value is under-predicted to -0.19. The experiment of Govardhan and Williamson published in Ma et al [45] also gives under-predicted value, the disagreement with Lourenco and Shih [27] is speculated to different aspect ratio. The experiment of Parnaudeau et al [43] has given an over-predicted value, as they pointed out that u_{min} may be more sensitive to the cylinder diameter, aspect ratio and blocking effect, The aspect ratio of Lourenco and Shih published in [27] was 20.5 while Govardhan and Williamson [45] was 10. From the numerical simulation side, it can be seen that different SGS model is not a deciding factor of the u_{min} value, see also in [28–31]. Rather, reducing the Rhie-Chow interpolation in PISO algorithm seem to have a bigger influence. Coming back to the 2nd point where different investigation disagrees, the location of the u_{min} is found at a big interval of (1D,2D) downstream. This area is

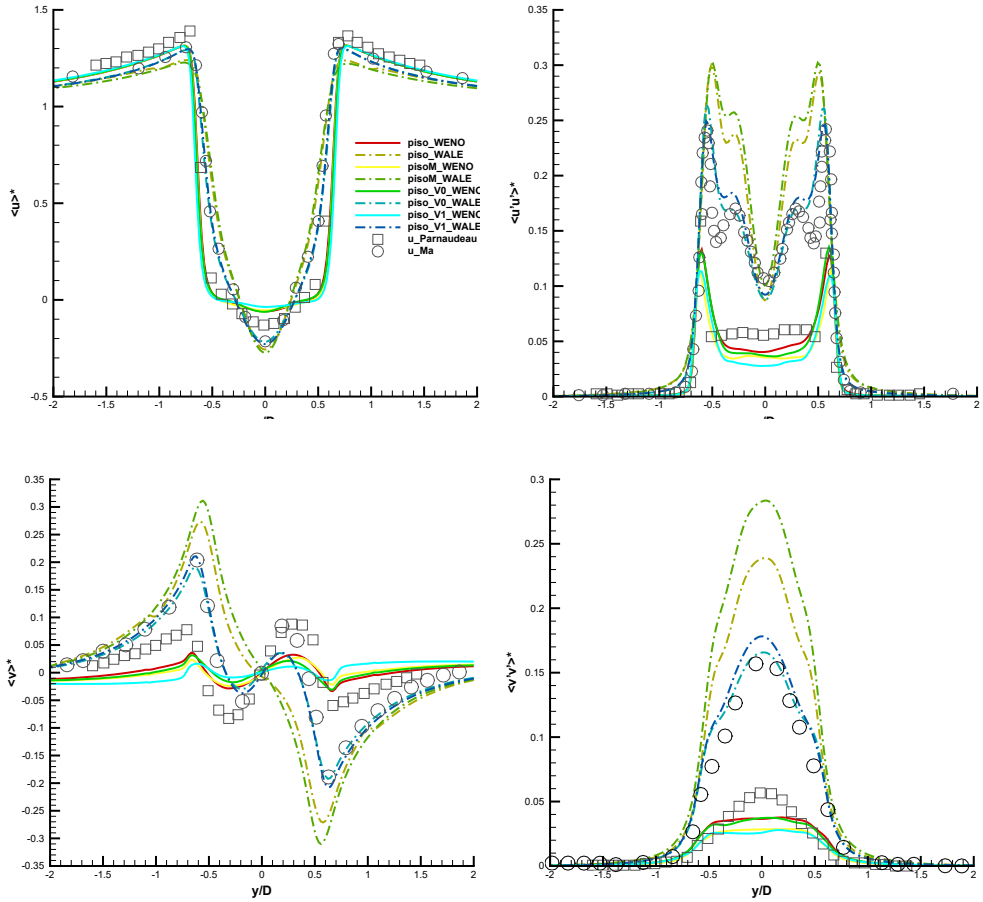

Fig. 7 Profiles of the normalized and time-averaged stream-wise velocity $\langle u \rangle$, the cross-section velocity $\langle v \rangle$ and their fluctuations $\langle u'u' \rangle$, $\langle v'v' \rangle$ at x=1.06, compared with the experiment data of Parnaudeau et al [43] and DNS of Ma et al [45].

known as the recirculation zone, where the most complex physics (of this test case) converge, such as the interactions of two separating shear layers and Von Karman vortex shedding. Norberg [51] pointed out there could be a transition between high and low vortex shedding mode. Further, the DNS study of Lehmkulh [15] suggested that the wake is shedding between these two modes alternatively, which possibly cause the large data scattering in the literature. More detailed discussion regarding the recirculation zone is made in the later section.

The fluctuation components are displayed in the right side of Figure 6, the global trend is in agreement for current results, the fluctuation quantity is first increasing from 0 to a max value near the end of the recirculation zone then tends to decay as further downstream. A double peak pattern was found by experiments of Norberg [53] and Parnaudeau et al [43], whereas no 2nd peak is found in current iLES/LES as well as in LES of Parnaudeau et al [43] and Tian and Xiao [31]. In DNS study of Lehmkulh et al [15], a single peak is detected in mode H while a double peak is identified in L mode. As pointed by Norberg [53], the first peak and the inflexion point might be linked to cross-over of mode B longitudinal vortices and Parnaudeau et al [43] noted that it is still difficult to clarify the correlation of the fluctuation peak to a specific vortical event. Here, the vortex formation length is defined as the distance between the cylinder base and the max value of fluctuation [54]. The transverse component $< v >^*$ does not seem to have a fixed pattern, it revealed a chaotic behaviour in the very near wake (x<2D), the clear oscillation can be observed further downstream, as the maxima and minima are switching, it is in consistence with a flow that is dominated by Von Karman vortex street. It should also be noticed that LES has a greater oscillation amplitude than iLES, as a consequence, a big fluctuation is also obtained.

In order to gain more insights in statistics of the wake, the velocities at location x=1.06D (very near wake) plotted in the Figure 7. For comparison in the very near wake, results from the DNS of Ma et al. [45] and experiment of

Parnaudeau et al. [43] are extracted.

A strong velocity deficit is found in the recirculation zone, a U shaped velocity profile is obtained in the very near wake at x=1.06 by iLES, a good agreement has been seen with experiment of Parnaudeau et al[43], meanwhile, a V shape is obtained by LES which is supported by DNS of Ma et al[45], also the results given by experiment of Lourenco and Shih[27] and LES of Kravechenko and Moin[42]. On the other hand, the co-existence of U and V shape is found by previous studies, examples are: V shape is found by iLES of Meyer et al[19] on Cartesian grid and U shape is produced on the Curvilinear grid, LES of Lysenco et al[29] using SMAG SGS model have shown a V shape and a U shape is obtained using TKE SGS model, Ma et al[45] found by doubling the spanwise size, the V shape turns to U shape. Chen et al[18] attribute the bifurcation to the numerical viscosity since they found both U and V shape can be obtained by adjusting the numerical viscosity. As in recent studies of [15, 18, 31], a U shape is more likely to appear if the numerical settings are consistent.

For the transverse component, the patterns given by current simulations are all antisymmetric with respect to y=0, which agrees well with references. The iLES results show an under-estimated profile at upstream near the cylinder but match well the experiments of Parnaudeau et al [43] and Ong et al [47] at downstream locations. The current LESs give good results compared to the DNS of Ma et al [45], with modified PISO solver, better results are obtained.

More variances and correlations can be seen from the fluctuation parts, on the right side of the Figure 7. At x=1.06, double strong peaks are captured for the stream-wise fluctuation, as a results of transitional state of shear layers, where a flapping behaviour is showed due to primary vortex formation [43]. The position of these two peaks are in agreement for current results and references, however, they differ from each other on the magnitude of the peak. The LES with standart Rhie-Chow interpolation have predicted the highest peak, with removal of Choi's correction, the magnitude remains with a slightly reduce step, as the reduction of R-C, the results match well with the DNS of Ma et al [45]. In the experiment of Parnaudeau et al [43], a smaller magnitude is obtained and a 'quiet' behaviour is showed inside the re-circulation zone, the current iLES have the similar results with a slightly under-estimated fluctuation inside the re-circulation zone.

D. Shedding Dynamics

In Figure 8 the instantaneous flow at the last time step is displayed. On the top left is from iLES and on the right is LES. Here, the process involving shear layer separating from surface, transition to turbulent (2D to 3D) can be observed. Due to excessive dissipation, LES predicts an early transition, smaller vortices are merging from the instability of separating shear layer which occurs closer to the cylinder, a more dis-ordered downstream flow structure, as a consequence, more oscillated lift and drag coefficients are produced. On the other hand, the property of laminar boundary layer is more retained for iLES, on the wake, the large and small scales are co-existing.

1. Vortex Shedding and Separation

Side view is showed on the bottom left of the Figure 8, one can see two boundary layers are separating from top and bottom of the cylinder, the primary vortex is forming by the rolling up of the separating boundary layer and small scale vortices, Von Karman vortex street is observed further downstream of vortex formation zone. The iLES predicted a longer vortex formation length than LES, as the separating boundary layer is becoming unstable at a further location. A view from top is displayed on the bottom right, dominating stream-wise vortices and alternative shedding pattern are observed respectively. The displayed instantaneous field has demonstrated a highly three-dimensional flow feature where the existence of multi-scale vortices are found. The shedding cycle consists of top boundary layer and bottom boundary rolling up alternatively (two opposite sign vortices shedding), this explains why the shedding frequency is half of the dominating drag frequency found is previous section. Overall, the flow visualisation is in agreement with Parnaudeau et al [43], Lysenko et al [29] and D'Alessandro et al [30].

2. One-Dimensional Velocity Spectras

To get more insights for the dynamics of the boundary layer instability and the wake, probes are replaced in several locations on the x-y plane, as demonstrated in Figure 9 and their coordinates on x-y plane is showed in Table 6. Probe 1 and Probe 2 are located on the wake centre-line at x=3D and x=5D respectively, reference data at these locations are from experiments of Ong and Wallace [47] and Parnaudeau et al [43] and they are re-scaled for the sake of clarity. The Kolmogorov dissipation law is represented by the dashed line with -5/3 slope in Figure 10. Probe 3 is placed at the location downstream near the separation point, Probe 4, Probe 5 and Probe 6 are located in the separating free-shear

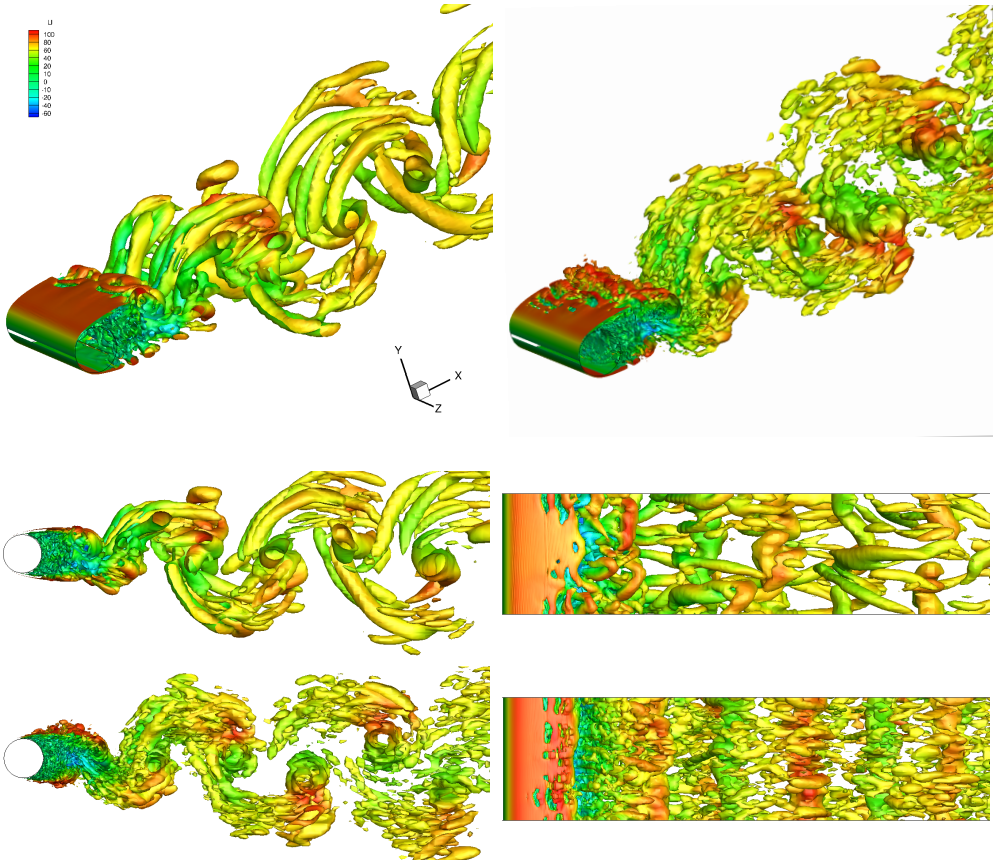

Fig. 8 Q criterion coloured by stream-wise velocity. The top left shows the visualisation of iLES and top right shows that of LES. More organised vortices are captured by the iLES.

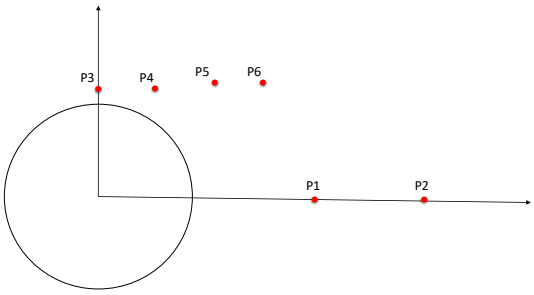

Fig. 9 probes locations

Probe	P1	P2	P3	P4	P5	P6
x/D	3	5	0	0.25	0.54	0.71
y/D	0	0	0.6	0.6	0.65	0.65

Table 6 Probes Locations in x-y plane: P1 and P2 are located in the wake region and P3-P6 are location in the separating boundary layer.

layer further downstream. For each probe, stream-wise and transverse velocities are evenly sampled for every time step $\Delta t = 0.000044$ and a total number of 91 000 samples (equivalent to 300 time units and over 60 shedding cycles) were collected during the course of each simulation, then the Hann window is used to perform FFT to obtain the velocity spectras. The shedding frequency of large-scale vortex (or Strouhal frequency) $f_s = 14.75hz \pm 1.3\%$ is used to get the non-dimentionlised frequency $f^* = f/f_s$, in accordance with the references.

In the Figure 10, the transverse velocity spectras obtained by various test cases at P1(x=3D) and P2(x=5D) in wake are showed, the overall numerical results agree well with previous experiments of Parnaudeau et al [43] and Ong and Wallace [47]. It can be observed that the narrow inertial subrange is well captured for current numerical schemes, where the -5/3 slope is satisfied. It is worth mention that rapid decaying spectras were noted in previous numerical studies of Ma et al [45] and Kravchenko and Moin [42], they found that no inertial range could be captured due to excessive numerical dissipation of the employed numerical method. However, the current good agreement with experiments may suggest that both LES and iLES approaches are not over-dissipative. Two peaks are very pronounced, where the fundamental peak at $f^* = 1$ corresponds to the Strouhal shedding frequency and its second harmonic peak is located at $f^* = 3$, however, its first harmonic peak at $f^* = 2$ is barely noticed by current and previous studies [29, 31, 43]. At higher frequency range where $f^* > 10$, the LES seems to be decaying faster than iLES but both spectras are in consistence with existing small scales far away downstream of the cylinder [42, 43], which can be observed in the visualisation showed in previous section (Figure 8). It should be also noted that the grid is coarser at Probe 2 which leads to a faster energy decay (narrower inertial subrange) than that at Probe 1. To conclude this paragraph, as can be seen on both probes, the inertial subrange is slightly broadened by removing the dissipative term from Choi's correction, but the impact in not obvious.

In the Figure 11, the stream-wise velocity spectras obtained by the probes inside the separating boundary layer are displayed. At Reynolds number greater than 1000, the separating boundary layer becomes unstable, then small scale vortices emerge from Kelvin-Helmholtz instabilities. The characteristic frequency f_{sl} which is associated with the instability is later labelled as shear layer frequency [55]. Before the formation of Von Karman vortex, as the result of shear-layer rolls up, these small vortices are gradually becoming visible as the Kelvin-Helmholtz instability is amplified. In practice, the characteristic frequency f_{sl} of the instability is normalised with the Strouhal shedding frequency f_s, by means of experiment, Prasad and Williamson [55] concluded a correlation frequency that $f_{sl}/f_s = 0.0235 \times Re^{0.67}$ implies $f_{sl}/f_s = 5.99$ for a Reynold number of 3900, in addition, the correlation indicates the characteristic frequency is higher as the Reynold number increases. In the following, ${f_{sl}}^*$ is used to denote the normalised shear layer frequency for simplicity.

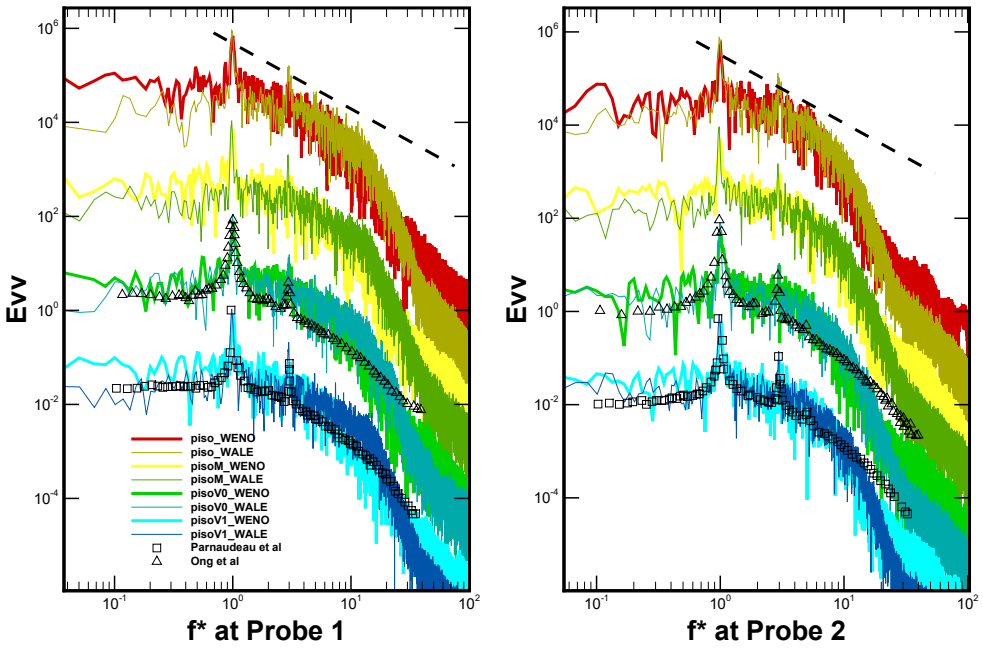

Fig. 10 transverse velocity spectras at probes P1(3,0), P2(5,0) in the wake, the dashed line is -5/3 slope

Case	Numerical Frame	P3	P4	P5	P6
Case 1	iLES piso	-	6.8	6.6	5.9
Case 2	LES piso	10.6	8.9	-	-
Case 3	iLES Mpiso	-	10.5	6.2	6.3
Case 4	LES Mpiso	10.6	8.9	-	-
Case 5	iLES pisoV0	-	6.5	6	6.1
Case 6	LES pisoV0	-	8.9	6	6.3
Case 7	iLES pisoV1	-	9.8	6.6	-
Case 8	LES pisoV1	-	8.9	6.6	6.1
Prasad and Williamson [55]	Experiment	5.99			
Dong et al. [49]	DNS	7.83			
Lehmkul et al. [15]	DNS	6.25			

Table 7 The shear layer frequency normalised with Strouhal frequency $f_{sl}{}^*$ at Probes P3-P6 and references

The Strouhal frequency f_s and its sub-harmonics are characterised by distinct sharp peaks, which are pronounced for all the Probes and test cases, whereas significant differences are found for normalised shear layer frequency $f_{sl}{}^*$. At Probe 3, only a weak 'bump' appears at $f^* = 10.6$ for Case 2 and even weaker for Case 4, it may suggest the instability is occurring at this location for these two cases. Further downstream at Probe 4, the broadened peak which is located in much higher frequency corresponds to shear layer frequency f_{sl}, the broadband also indicates the small vortices are occurring in a wide range of frequencies, contrary to Strouhal frequency f_s that only characterised by sharp peaks. Contrary to LES results, the shear layer frequency f_{sl} predicted by iLES is much less pronounced. At Probe 5, the broadened peak seems to be vanished for Case 2 and Case 4, whereas for iLES cases, apart from Case 7, the f_{sl} is clearly observed. At the furthest Probe 6, the shear layer frequency are becoming less pronounced for Case 6 and Case 8, meanwhile, the spectral distribution for iLES cases remain the same as previous probe. The predicted normalised shear layer frequency $f_{sl}{}^*$ for all test cases are summarised in Table 7, which are generally in good agreement with DNS of Dong et al [49] who gives $f_{sl}{}^* = 7.83$ and Lehmkul et al [15] where $f_{sl}{}^* = 6.25$, as well as Prasad and Williamson [55] who first concluded the $f_{sl}{}^* = 5.99$, but the values given by iLES are closer to references while LES predicted a slightly greater value.

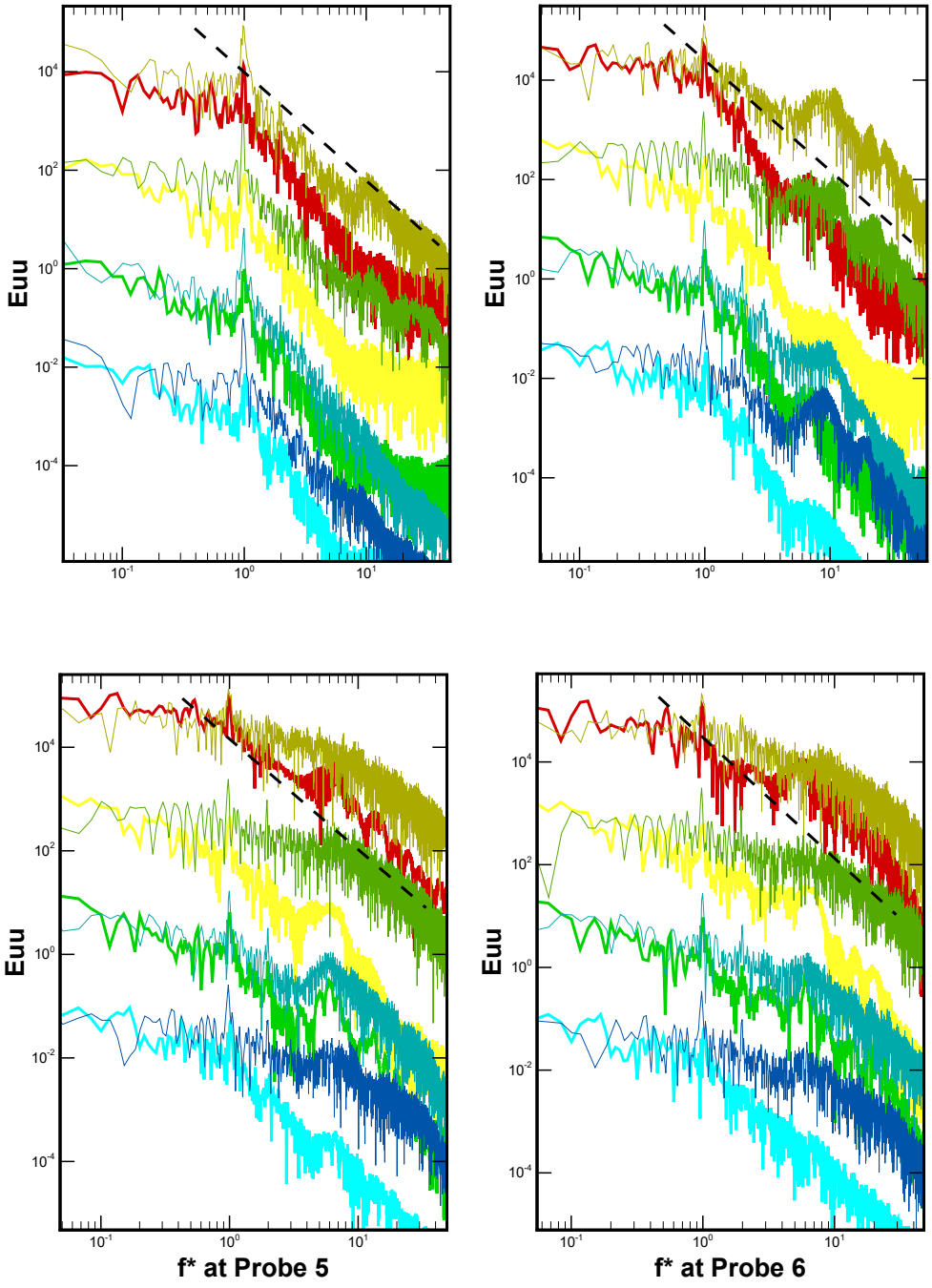

Fig. 11 stream-wise velocity spectras at probes P3(0,0.6), P4(0.25,0.6), P5(0.54,0.65), P6(0.71,0.65) in the separating boundary layer, the dashed line is the -5/3 slope

Here it is worth emphasising that, as discussed previously, LES cases predicted the shortest recirculation length due to the early transition of the separating boundary layer, the effect of the Rhie-Chow interpolation weighting is found particularly obvious on the stream-wise velocity spectras obtained by LES. The less Rhie-Chow interpolation, the later the instability in the separating boundary layer occurs. On the other hand, there is very limited impact for iLES, except for the Rhie-Chow interpolation is reduced to a small level (Case 7), where the shear layer frequency almost remains barely noticeable for all the probes. Overall, the shear layer frequency is becoming weaker as the 2 dimensional shear layer breaks down forming 3 dimensional vortices downstream, therefore the broadband frequency tends to disappear, the observations are consistent with those of Dong et al [49].

V. Conclusion

In the current work, extensive investigation of implicit and conventional LES coupling with various modified PISO algorithms is carried out. The separated flow around circular cylinder at a Reynolds number of 3900 is studied. Numerical simulations are performed on wall resolving grids with 0.9×10^6 and 3.6×10^6 finite volume cells, the span-wise resolution is fixed in accordance with the literature [15, 18, 29–31], the overall results are within the good range of previous numerical and experimental studies.

At the transitional range of Reynolds number, the bifurcation of stream-wise velocity profile at the very near wake x=1.06D is confirmed by current numerical simulations, where the conventional LES predicted a V shape and iLES predicted a U shape. The re-circulation length is one of the most important parameter in the current flow configuration, although large scarceness of reference data from literature is found. The current iLES predicted a slightly longer recirculation length compared to the averaged length from the literature, while conventional LES significantly under-predicted the length. The back base pressure and drag coefficient are consistent with references, despite the value computed by conventional LES being slightly bigger that that of iLES, in addition, a much higher oscillation magnitude of lift coefficient is obtained. The analysis of velocity spectras revealed the Kelvin-Helmholtz instability in the separating shear layer occurs earlier for simulations using conventional LES due to its higher-dissipative property than iLES, as a result, iLES captures better Von Karman vortex structures than conventional LES in the downstream of the wake.

The current iLES conducted within OpenFOAM has a non-dissipative property, the overall physical parameters are predicted reasonably well compared to high fidelity references, furthermore, it has similar numerical behaviour to the LES of Lysenko et al [29] and LES of Ouvrard et al [50], indicating the reliability of leading truncation error term of the current unstructured 3rd order WENO scheme can be employed as an implicit SGS model. Meanwhile, it should be noted a 3rd order WENO scheme iLES is still more expensive than conventional LES. For conventional LES approach, the initial results reveal the non-negligible impact of Rhie-Chow interpolation, the prediction of the wake statistics can be improved by gradually limiting the Rhie-Chow interpolation.

Acknowledgments

This research has extensively employed the Cranfield University High Performance Computing (HPC) facility. The authors would like to acknowledge the support and guidance received from Dr Mick Knaggs at the Cranfield HPC department.

References

[1] Chapman, D., "Computational Aerodynamics Development and Outlook," *AIAA Journal*, Vol. 17, No. 12, 1979, pp. 1293–1313. https://doi.org/10.2514/6.1979-129.

[2] Choi, H., and Moin, P., "Grid-point requirements for large eddy simulation: Chapman's estimates revisited," *Physics of Fluids*, Vol. 24, No. 1, 2012. https://doi.org/10.1063/1.3676783.

[3] Drikakis, D., Fureby, C., Grinstein, F. F., and Youngs, D., "Simulation of transition and turbulence decay in the Taylor-Green vortex," *Journal of Turbulence*, Vol. 8, 2007, pp. 1–12. https://doi.org/10.1080/14685240701250289.

[4] Boris, J. P., "On large eddy simulation using subgrid turbulence models Comment," *Whither Turbulence ? or Turbulence at the Crossroads*, 1990, pp. 344–353. https://doi.org/10.1007/3-540-52535-1_53.

[5] Boris, J. P., Grinstein, F. F., Oran, E. S., and Kolbe, R. L., "New insights into large eddy simulation," *Fluid Dynamics Research*, Vol. 10, No. 4-6, 1992, pp. 199–228. https://doi.org/10.1016/0169-5983(92)90023-P.

[6] Grinstein, F. F., Margolin, L. G., and Rider, W. J., *Implicit Large Eddy Simulation: computing turbulent fluid dynamics*, Cambridge University Press, 2007.

[7] Liu, X. D., Osher, S., and Chan, T., "Weighted Essentially Non-Oscillatory Schemes," *Journal of Computational Physics*, 1994, pp. 200–212.

[8] Hahn, M., "Implicit Large-Eddy Simulation of Low-Speed Separated Flows Using High-Resolution Methods," Ph.D. thesis, 2008.

[9] Dumbser, M., and Käser, M., "Arbitrary high order non-oscillatory finite volume schemes on unstructured meshes for linear hyperbolic systems," *Journal of Computational Physics*, Vol. 221, No. 2, 2007, pp. 693–723. https://doi.org/10.1016/j.jcp.2006.06.043.

[10] Tsoutsanis, P., Titarev, V. A., and Drikakis, D., "WENO schemes on arbitrary mixed-element unstructured meshes in three space dimensions," *Journal of Computational Physics*, Vol. 230, No. 4, 2011, pp. 1585–1601. https://doi.org/10.1016/j.jcp.2010.11.023, URL http://dx.doi.org/10.1016/j.jcp.2010.11.023.

[11] Tsoutsanis, P., Antoniadis, A. F., and Drikakis, D., "WENO schemes on arbitrary unstructured meshes for laminar, transitional and turbulent flows," *Journal of Computational Physics*, Vol. 256, 2014, pp. 254–276. https://doi.org/10.1016/j.jcp.2013.09.002, URL http://dx.doi.org/10.1016/j.jcp.2013.09.002.

[12] Zeng, K., Li, Z., Rana, Z. A., and Jenkins, K. W., "Implicit Large Eddy Simulations of Turbulent Flow around a Square Cylinder at Reynolds Number of 22 000," *Computers and Fluids*, Vol. 226, 2021, p. 105000. https://doi.org/10.1016/j.compfluid.2021.105000, URL https://doi.org/10.1016/j.compfluid.2021.105000.

[13] Martin, T., and Shevchuk, I., "Implementation and Validation of Semi-Implicit WENO Schemes Using OpenFOAM®," *Computation*, Vol. 6, No. 1, 2018, p. 6. https://doi.org/10.3390/computation6010006.

[14] Wissink, J. G., and Rodi, W., "Numerical study of the near wake of a circular cylinder," *International Journal of Heat and Fluid Flow*, Vol. 29, No. 4, 2008, pp. 1060–1070. https://doi.org/10.1016/j.ijheatfluidflow.2008.04.001.

[15] Lehmkuhl, O., Rodríguez, I., Borrell, R., and Oliva, A., "Low-frequency unsteadiness in the vortex formation region of a circular cylinder," *Physics of Fluids*, Vol. 25, No. 8, 2013. https://doi.org/10.1063/1.4818641.

[16] Smith, T. A., and Ventikos, Y., "Boundary layer transition over a foil using direct numerical simulation and large eddy simulation," *Physics of Fluids*, Vol. 31, No. 12, 2019. https://doi.org/10.1063/1.5126663, URL https://doi.org/10.1063/1.5126663.

[17] Franke, J., and Frank, W., "Large eddy simulation of the flow past a circular cylinder at ReD = 3900," *Journal of Wind Engineering and Industrial Aerodynamics*, Vol. 90, No. 10, 2002, pp. 1191–1206. https://doi.org/10.1016/S0167-6105(02)00232-5.

[18] Chen, H., Li, Z., and Yufei, Z., "U or v Shape: Dissipation effects on cylinder flow implicit large-eddy simulation," *AIAA Journal*, Vol. 55, No. 2, 2017, pp. 459–473. https://doi.org/10.2514/1.J055278.

[19] Meyer, M., Hickel, S., and Adams, N. A., "Assessment of Implicit Large-Eddy Simulation with a Conservative Immersed Interface Method for turbulent cylinder flow," *International Journal of Heat and Fluid Flow*, Vol. 31, No. 3, 2010, pp. 368–377. https://doi.org/10.1016/j.ijheatfluidflow.2010.02.026, URL http://dx.doi.org/10.1016/j.ijheatfluidflow.2010.02.026.

[20] Expósito, D., and Rana, Z. A., "Computational investigations into heat transfer over a double wedge in hypersonic flows," *Aerospace Science and Technology*, Vol. 92, 2019, pp. 839–846. https://doi.org/10.1016/j.ast.2019.07.013, URL https://doi.org/10.1016/j.ast.2019.07.013.

[21] Rhie, C., and Chow, W., "A numerical study of the turbulent flow past an isolated airfoil with trailing edge separation," *3rd Joint Thermophysics, Fluids, Plasma and Heat Transfer Conference*, 1982. https://doi.org/10.2514/6.1982-998, URL http://arc.aiaa.org/doi/10.2514/6.1982-998.

[22] Jasak, H., "Error Analysis and Estimation for the finite volume method with applications to fluid flows," Ph.D. thesis, 1996.

[23] Komen, E. M., Camilo, L. H., Shams, A., Geurts, B. J., and Koren, B., "A quantification method for numerical dissipation in quasi-DNS and under-resolved DNS, and effects of numerical dissipation in quasi-DNS and under-resolved DNS of turbulent channel flows," *Journal of Computational Physics*, Vol. 345, 2017, pp. 565–595. https://doi.org/10.1016/j.jcp.2017.05.030, URL http://dx.doi.org/10.1016/j.jcp.2017.05.030.

[24] Vuorinen, V., Keskinen, J. P., Duwig, C., and Boersma, B. J., "On the implementation of low-dissipative Runge-Kutta projection methods for time dependent flows using OpenFOAM®," *Computers and Fluids*, Vol. 93, 2014, pp. 153–163. https://doi.org/10.1016/j.compfluid.2014.01.026, URL http://dx.doi.org/10.1016/j.compfluid.2014.01.026.

[25] Choi, S. K., "Note on the use of momentum interpolation method for unsteady flows," *Numerical Heat Transfer; Part A: Applications*, Vol. 36, No. 5, 1999, pp. 545–550. https://doi.org/10.1080/104077899274679.

[26] Yu, B., Tao, W., Wei, J., Kawaguchi, Y., Tagawa, T., and Ozoe, H., "Discussion on Momentum Interpolation Method for Collocated Grids of Incompressible Flow," *Numerical Heat Transfer*, Vol. Part B, No. 42, 2002, pp. 141–166.

[27] Beaudan, P., and Moin, P., "Numerical experiments on the flow past a circular cylinder at sub-critical Reynolds number," *Stanford University*, , No. Report No. TF-62, 1994, pp. 1–262.

[28] Breuer, M., "Large eddy simulation of the subcritical flow past a circular cylinder: Numerical and modeling aspects," *International Journal for Numerical Methods in Fluids*, Vol. 28, No. 9, 1998, pp. 1281–1302. https://doi.org/10.1002/(sici)1097-0363(19981215)28:9<1281::aid-fld759>3.0.co;2-23.

[29] Lysenko, D. A., Ertesvåg, I. S., and Rian, K. E., "Large-Eddy Simulation of the Flow Over a Circular Cylinder at Reynolds Number 3900 Using the OpenFOAM Toolbox," *Flow, Turbulence and Combustion*, Vol. 89, No. 4, 2012, pp. 491–518. https://doi.org/10.1007/s10494-012-9405-0.

[30] D'Alessandro, V., Zoppi, A., Binci, L., and Ricci, R., "Development of openfoam solvers for incompressible navier–stokes equations based on high-order runge–kutta schemes," *International Journal of Computational Methods and Experimental Measurements*, Vol. 4, No. 4, 2016, pp. 594–603. https://doi.org/10.2495/CMEM-V4-N4-594-603, URL http://www.witpress.com/journals/CMEM-594-603.

[31] Tian, G., and Xiao, Z., "New insight on large-eddy simulation of flow past a circular cylinder at subcritical Reynolds number 3900," *AIP Advances*, Vol. 10, No. 8, 2020. https://doi.org/10.1063/5.0012358, URL https://doi.org/10.1063/5.0012358.

[32] Nicoud, F., and Ducros, F., "Subgrid-Scale Stress Modelling Based on the Square of the Velocity Gradient Tensor," *Flow, Turbulence and Combustion*, Vol. 62, 1999, pp. 183–200. https://doi.org/10.1016/j.jcp.2004.10.018.

[33] Moukalled, F., Mangani, L., and Darwish, M., *The Finite Volume Method in Computational Fluid Dynamics*, Vol. 113, 2016. https://doi.org/10.1007/978-3-319-16874-6, URL http://www.scopus.com/inward/record.url?eid=2-s2.0-84939129919&partnerID=tZOtx3y1.

[34] Asada, K., and Kawai, S., "Revisiting LESFOIL: Wall-resolved LES of Flow Around an Airfoil at Reynolds number of 2 100 000," *2018 AIAA Aerospace Sciences Meeting*, , No. January, 2018, pp. 1–18. https://doi.org/10.2514/6.2018-0840, URL https://arc.aiaa.org/doi/10.2514/6.2018-0840.

[35] Castiglioni, G., and Domaradzki, J. A., "A numerical dissipation rate and viscosity in flow simulations with realistic geometry using low-order compressible Navier-Stokes solvers," *Computers and Fluids*, Vol. 119, 2015, pp. 37–46. https://doi.org/10.1016/j.compfluid.2015.07.004, URL http://dx.doi.org/10.1016/j.compfluid.2015.07.004.

[36] Issa, R. I., "Solution of the implicitly discretised fluid flow equations by operator-splitting," *Journal of Computational Physics*, Vol. 62, No. 1, 1986, pp. 40–65. https://doi.org/10.1016/0021-9991(86)90099-9.

[37] Modesti, D., and Pirozzoli, S., "A low-dissipative solver for turbulent compressible flows on unstructured meshes, with OpenFOAM implementation," *Computers and Fluids*, Vol. 152, 2017, pp. 14–23. https://doi.org/10.1016/j.compfluid.2017.04.012.

[38] D'Alessandro, V., Binci, L., Montelpare, S., and Ricci, R., "On the development of OpenFOAM solvers based on explicit and implicit high-order Runge–Kutta schemes for incompressible flows with heat transfer," *Computer Physics Communications*, Vol. 222, 2017, pp. 14–30. https://doi.org/10.1016/j.cpc.2017.09.009, URL http://dx.doi.org/10.1016/j.cpc.2017.09.009.

[39] Komen, E., Shams, A., Camilo, L., and Koren, B., "Quasi-DNS capabilities of OpenFOAM for different mesh types," *Computers and Fluids*, Vol. 96, 2014, pp. 87–104. https://doi.org/10.1016/j.compfluid.2014.02.013, URL http://dx.doi.org/10.1016/j.compfluid.2014.02.013.

[40] Johansson, P., and Davidson, L., "Modified collocated simplec algorithm applied to buoyancy-affected turbulent flow using a multigrid solution procedure," *Numerical Heat Transfer, Part B: Fundamentals*, Vol. 28, No. 1, 1995, pp. 39–57. https://doi.org/10.1080/10407799508928820.

[41] Montecchia, M., Brethouwer, G., Wallin, S., Johansson, A. V., and Knacke, T., "Improving LES with OpenFOAM by minimising numerical dissipation and use of explicit algebraic SGS stress model," *Journal of Turbulence*, Vol. 20, No. 11-12, 2019, pp. 697–722. https://doi.org/10.1080/14685248.2019.1706740.

[42] Kravchenko, A., and Moin, P., "Numerical simulation of flow over a circular cylinder at low Reynolds number," *Physics of Fluids*, Vol. 12, 2000. https://doi.org/10.4028/www.scientific.net/AMR.255-260.942.

[43] Parnaudeau, P., Carlier, J., Heitz, D., and Lamballais, E., "Experimental and numerical studies of the flow over a circular cylinder at Reynolds number 3900," *Physics of Fluids*, Vol. 20, No. 8, 2008. https://doi.org/10.1063/1.2957018.

[44] Tsoutsanis, P., and Dumbser, M., "Arbitrary high order central non-oscillatory schemes on mixed-element unstructured meshes," *Computers and Fluids*, Vol. 225, 2021, p. 104961. https://doi.org/10.1016/j.compfluid.2021.104961, URL https://doi.org/10.1016/j.compfluid.2021.104961.

[45] Ma, X., Karamanos, G. S., and Karniadakis, G. E., "Dynamics and low-dimensionality of a turbulent near wake," *Journal of Fluid Mechanics*, Vol. 410, 2000, pp. 29–65. https://doi.org/10.1017/S0022112099007934.

[46] Norberg, C., "An experimental investigation of the flow around a circular cylinder: Influence of aspect ratio," *Journal of Fluid Mechanics*, Vol. 258, 1994, pp. 287–316. https://doi.org/10.1017/S0022112094003332.

[47] Ong, L., and Wallace, J., "The velocity field of the turbulent very near wake of a circular cylinder," *Experiments in Fluids*, Vol. 20, No. 6, 1996, pp. 441–453. https://doi.org/10.1007/BF00189383.

[48] Spalart, P. R., Jou, W., Strelets, M., and Allmaras, S., "Comments on the feasibility of LES for wings, and on a hybrid RANS/LES approach," *First AFOSR International Conference on DNS/LES, Ruston, LA, 4–8, August, 1997, in Advances in DNS/LES, edited by C. Liu and Z. Liu*, 1997.

[49] Dong, S., Karniadakis, G. E., Ekmekci, A., and Rockwell, D., "A combined direct numerical simulation-particle image velocimetry study of the turbulent near wake," *Journal of Fluid Mechanics*, Vol. 569, 2006, pp. 185–207. https://doi.org/10.1017/S0022112006002606.

[50] Ouvrard, H., Koobus, B., Dervieux, A., and Salvetti, M. V., "Classical and variational multiscale LES of the flow around a circular cylinder on unstructured grids," *Computers and Fluids*, Vol. 39, No. 7, 2010, pp. 1083–1094. https://doi.org/10.1016/j.compfluid.2010.01.017, URL http://dx.doi.org/10.1016/j.compfluid.2010.01.017.

[51] Norberg, C., "Fluctuating lift on a circular cylinder: Review and new measurements," *Journal of Fluids and Structures*, Vol. 17, No. 1, 2003, pp. 57–96. https://doi.org/10.1016/S0889-9746(02)00099-3.

[52] Rodi, W., Ferziger, J. H., Breuer, M., and Pourquié, M., "Status of large eddy simulation: Results of a workshop," *Journal of Fluids Engineering, Transactions of the ASME*, Vol. 119, No. 2, 1997, pp. 248–262. https://doi.org/10.1115/1.2819128.

[53] Norberg, C., "LDV-measurements in the near wake of a circular cylinder Experimental Details," *Proceedings ofthe Conference on BluffBody Wakes and Vortex-Induced Vibration, Washington, D.C*, 1998, pp. 1–12.

[54] Williamson, C. H., "Vortex dynamics in the cylinder wake," *Annual Review of Fluid Mechanics*, Vol. 28, 1996, pp. 477–539. https://doi.org/10.1146/annurev.fl.28.010196.002401.

[55] Prasad, A., and Williamson, C. H., "The instability of the shear layer separating from a bluff body," *Journal of Fluid Mechanics*, Vol. 333, 1997, pp. 375–402. https://doi.org/10.1017/S0022112096004326.

2024-01-04

Implicit and conventional large eddy simulation of flow around a circular cylinder at Reynolds number of 3900

Li, Zhuoneng

AIAA

Li Z, Da Ronch A, Rana ZA, Jenkins K. (2024) Implicit and conventional large eddy simulation of flow around a circular cylinder at Reynolds number of 3900. In AIAA SCITECH 2024 Forum, 8-12 January 2024, Orlando, FL, USA, Article Number 2024-0064

https://doi.org/10.2514/6.2024-0064